Strategy for Wettability Modification Through High-Aspect Ratio Texturing Using Picosecond Direct Laser Interference Patterning

Fabian Ränke*[1], Marcelo Sallese[1], Marcos Soldera[1], Mayla Barrientos[1], Agustin Götte[1], and Andrés F. Lasagni[1,2]

[1] *Institute of Manufacturing Technology, Technische Universität Dresden, George-Bähr-Str. 3c ,01069 Dresden, Germany*

[2]*Fraunhofer-Institut für Werkstoff- und Strahltechnik, Winterbergstr. 22. 01277 Dresden, Germany*

**Fabian.raenke@tu-dresden.de.*

Direct Laser Interference Patterning (DLIP) has become an industrial-relevant method for microtexturing materials and modifying surface properties. Despite extensive research on DLIP-processed metals for hydrophobicity, the long-term effects of texture geometry on static and dynamic wetting are not yet fully understood. Here, periodic microstructures on stainless steel were fabricated by ps-DLIP to study the effects of texture type, spatial period Λ, and aspect ratio AR on the surface wettability. Line- and cross-like textures with Λ = 6.0, 10.0, and 30.0 µm were created using a multi-scan approach to reach ARs of 0.3, 0.6, and 1.0. Wettability was monitored over 220 days by measuring static water contact angle (WCA), contact angle hysteresis (CAH), roll-off angle ($\theta_{Roll\text{-}off}$), and surface free energy (SFE). The results show that smaller spatial periods (6.0 and 10.0 µm) favored superhydrophobicity (WCA > 150°), with faster stabilization times. In turn, patterns with Λ = 30.0 µm exhibited a rose-petal effect, with WCA up to 143.4° and CAH > 45°. All structured surfaces showed a decrease of the polar component of SFE, in alignment with the observed water-repellency properties. Overall, the period proved to be the dominant factor for increasing the long-term hydrophobicity through DLIP.

DOI: 10.2961/ilmn.2025.02.2006

Keywords: Direct Laser Interference Patterning, high aspect ratio structures, wettability, stainless steel

1. Introduction

Stainless steel is a widely used material across numerous industries, including automotive, medical, and food processing, due to its excellent mechanical properties and corrosion resistance [1]. However, to expand its functionality, especially in applications involving liquid interaction, modifying its surface wettability has become increasingly important. The ability to control how liquids interact with solid surfaces is critical for enabling functions such as self-cleaning [2–4], anti-fogging [5–7], and enhanced corrosion resistance [8, 9]. A classic natural model for controlled wettability is the lotus leaf, whose hierarchical micro- and nanostructures yield remarkable water repellency and self-cleaning properties [10]. Inspired by such biological surfaces, researchers have focused on replicating these wetting behaviors through engineered surface texturing techniques.

In this context, laser-based techniques have emerged as a promising technology for replicating these surface properties by creating complex periodic microstructures on metals in a single process step [11–13]. Among these techniques, Direct Laser Interference Patterning (DLIP), stands out for its distinct advantages over conventional Direct Laser Writing (DLW) methods, including smaller feature sizes coupled with higher processing rates [14–16].

DLIP is based on the overlap of multiple laser beams in the focal plane to create an interference pattern with a periodic distribution of laser intensity. The geometry of the resulting interference pattern depends on the number of interfering beams, the individual angle of incidence as well as phase and polarization of each laser beam [17]. Therefore, this technique offers a wide range of different surface structures [18]. Through the utilization of ultra-short laser pulses, the material can be locally heated only at the interference maxima positions, reducing the amount of undesired molten material and allowing the fabrication of highly homogeneous patterns with feature sizes even in the sub-micrometer range [19]. Moreover, when using ultrashort pulses on metallic substrates, self-organized nano- and microstructures, commonly known as Laser-Induced Periodic Surface Structures (LIPSS), arise in combination with the produced DLIP features and thus leading to the formation of multi-scale textures [20–24].

In the past, DLIP has been successfully used to tune the wettability of stainless-steel substrates, by the production of periodic micro-structures [25–28]. For instance, Schell et al. employed a nanosecond four-beam DLIP setup to fabricate periodic dot-like microstructures with different initial roughness to investigate the influence of the fabricated surface pattern on the wetting behavior and its temporal evolution [29]. Furthermore, Aguilar-Morales et al. used a picosecond

two beam DLIP set up to produce high aspect ratio line- and cross-like DLIP structures, which demonstrated a high degree of hydrophobicity by applying a single scan coupled with overlaps up to 99 %. The obtained results also pointed out that the hierarchical surface structure composed of cross-like DLIP and LIPSS, led to higher contact angles compared to single-scale microstructures [28]. In this direction, Shimada et al. used a femtosecond DLIP setup based on a spatial light modulator to fabricate shallow single and multiscale line-like structures with different spatial periods. The results suggested that hierarchical DLIP topographies were more stable and showed better reproducibility for the static WCA over compared to single scale texture [30].

Despite these advances, a comprehensive understanding of how geometric parameters of the texture (spatial period, aspect ratio and pattern shape) influence the long-term evolution of wetting properties remains limited. Previous studies have focused primarily on short-term static water contact angles (WCA) measurements, often neglecting complementary parameters like contact angle hysteresis (CAH), roll-off angle, and surface free energy (SFE), which are essential for evaluating dynamic wetting and predicting self-cleaning performance.

This study addresses this gap by systematically investigating the effects of spatial period (Λ = 6.0, 10.0, 30.0 µm), aspect ratio (AR = 0.3, 0.6, 1.0), and texture geometry (line- and cross-like) on the wettability characteristics of stainless steel (SS1.4301) surfaces structured using picosecond DLIP. The long-term wettability is studied over 220 days by measuring static WCA, while the dynamic wetting behavior is evaluated through CAH and roll-off angle experiments. In addition, to a gain deeper insight into the chemical and physical interactions between the treated surfaces and liquids, surface free energy measurements are conducted using liquids of opposing polarities. The SFE measurements complement contact angle analysis by differentiating between polar and dispersive interactions. By correlating structural parameters with temporal and functional wetting behavior, this work aims to provide a more detailed understanding of how to engineer durable, application-specific wetting properties using DLIP.

2. Materials and methods

2.1 Materials

For the laser structuring experiments, X5CrNi18-10 plates (SS 1.4301) were utilized with dimensions of 60 mm × 90 mm × 0.8 mm and an average surface roughness (Sa) of 50 nm. Prior to the laser treatment, the metallic samples were cleaned with absolute ethanol (99.9%, Supelco, Germany) to remove any possible contamination. Subsequently, the substrates were dried with compressed air.

2.2 Ps-DLIP process

The laser texturing was performed employing an optical configuration with two-beam interference optics. The experimental setup consists of a picosecond solid-state laser (Innoslab PX, EdgeWave, Germany) delivering laser pulses with a pulse duration of 12 ps and a maximal average laser power of 60 W. The infrared laser beam (λ = 1064 nm) was expanded using a two-lens telescope system and directed into an optical DLIP head (ELIPSYS®, SurFunction GmbH, Germany - EU patent EP3990211B1). There, a Diffractive Optical Element (DOE) splits the main beam into two sub-beams, which are subsequently shaped into an elongated spot (**Figure 1a**)

This optical head enables an impressive depth of focus of ~ 10 mm and generates an elliptically shaped laser spot with dimensions ($d_x \times d_y$) of 1.03 ± 0.06 × 0.09 ± 0.01 mm^2 at the focal plane. The spatial period (Λ) of the interference pattern can be calculated considering the interference angle (Θ) (**Figure 1a**) as well as the laser wavelength (λ), using equation (1):

$$\Lambda = \frac{\lambda}{2 \cdot sin(\frac{\theta}{2})}. \quad (1)$$

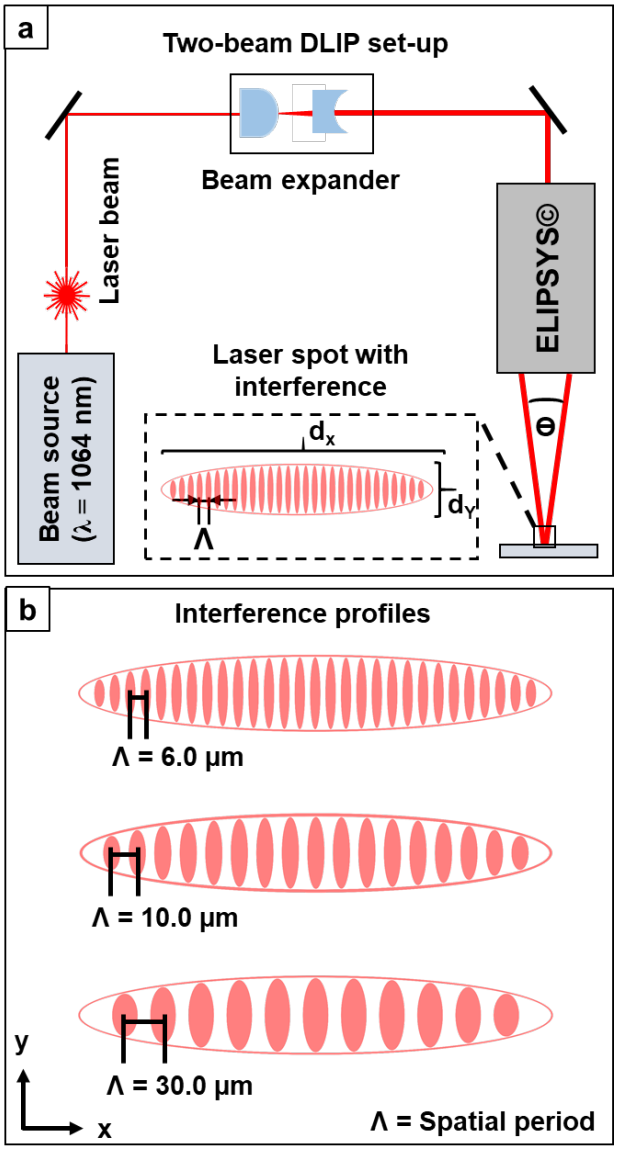

Fig. 1 (a) Schematic drawing of the experimental setup showing the two-beam DLIP optical configuration provided by ELIPSYS® head. The inset denotes the two overlapping sub-beams producing a line-like distribution of laser intensity. (b) Resulting interference profiles for spatial periods Λ = 6.0, 10.0, 30.0 µm.

For this study the texture spatial period was changed by exchanging the DOE within the optical configuration, so that spatial periods of 6.0, 10.0, and 30.0 µm could be produced (**Figure 1b**).

The motion of the metallic substrates in two-dimensional directions was realized with mechanical stages (Aerotech PRO155-05, USA). Considering the size of the laser spot in the y-direction and the used pulse-to-pulse distance, it is possible to calculate the Pulse-to-Pulse Overlap (OV) by using equation (2):

$$OV = \left(1 - \frac{PtP}{d_y}\right) \times 100\%. \quad (2)$$

The surfaces were textured at a fixed repetition rate (f_{rep}) of 10 kHz and OV of 90% and 95%. For the treatment of large areas, the hatch distance, which is the lateral distance (x-direction according to Figure 1b) between structured tracks, was set in dependence of the employed spatial period.

In order to produce cross-like features, the metallic samples were first processed to create a line-like DLIP pattern and subsequently rotated 90° in the x-y plane and re-irradiated using the same process parameters. The laser experiments were carried out in ambient environment with no additional treatment.

2.3 Topographical analysis

For evaluating the surface topography of the laser-structured samples, White Light Interferometric (WLI) images (Sensofar S-Neox, Spain) were recorded by employing 50x magnification objective providing vertical of 1 nm and lateral resolutions of 500 nm, respectively. The surface profiles and average structure depth values were obtained using the SensoMAP Advanced Analysis Software (Sensofar, Spain). High resolution images were recorded using Scanning Electron Microscopy (SEM) operating at an acceleration voltage of 12 kV (Quattro ESEM, Thermo Fischer Scientific, Germany).

2.4 Wettability analysis

The wettability was characterized by static water contact angle measurements using deionized water with droplet volume of 5 µL. The calculation of the contact angle was conducted with the water contact angle system DSA100 (KRÜSS GmbH, Germany) employing the tangent method. The WCA of the laser-structured surfaces was continuously monitored for 220 days. Directly after the laser treatment, the samples were stored under ambient conditions.

Additionally, the static contact angle hysteresis was determined 220 days after laser texturing by measuring the advancing and receding water contact angle of an inflating and deflating water droplet on the laser-textured surfaces. After an initial droplet with a volume of 5 µL was deposited, a liquid volume of 10 µL was subsequently dispensed at a dosing rate of 0.5 µL s^{-1}. The advancing contact angle (θ_{Adv}) was recorded at 1.0 s intervals. After the droplet reached the steady state, the receding contact angle (θ_{Rec}) was then measured by re-absorbing the water with the syringe under same conditions. The procedure finished when the droplet detached from the sample surface.

In addition, the roll-off angle ($\theta_{Roll\text{-}off}$) was determined by placing a droplet on the laser-treated samples and incrementally tilting the sample angle from 0° to 50° in 1° steps. Furthermore, the Owens-Wendt-Rabel-Kaelbel (OWRK) approach was used to determine the surface free energy of the laser-textured substrates by measuring the static contact angles of a polar (deionized water) and non-polar (diiodomethane) liquid [31,32]. All measurements were performed employing a droplet volume of 5 µL, each measurement was repeated five times for statistical significance. The surface free energy for the two testing liquids used in this study, as well as their dispersive γD and polar γP components are given in **Table 1.**

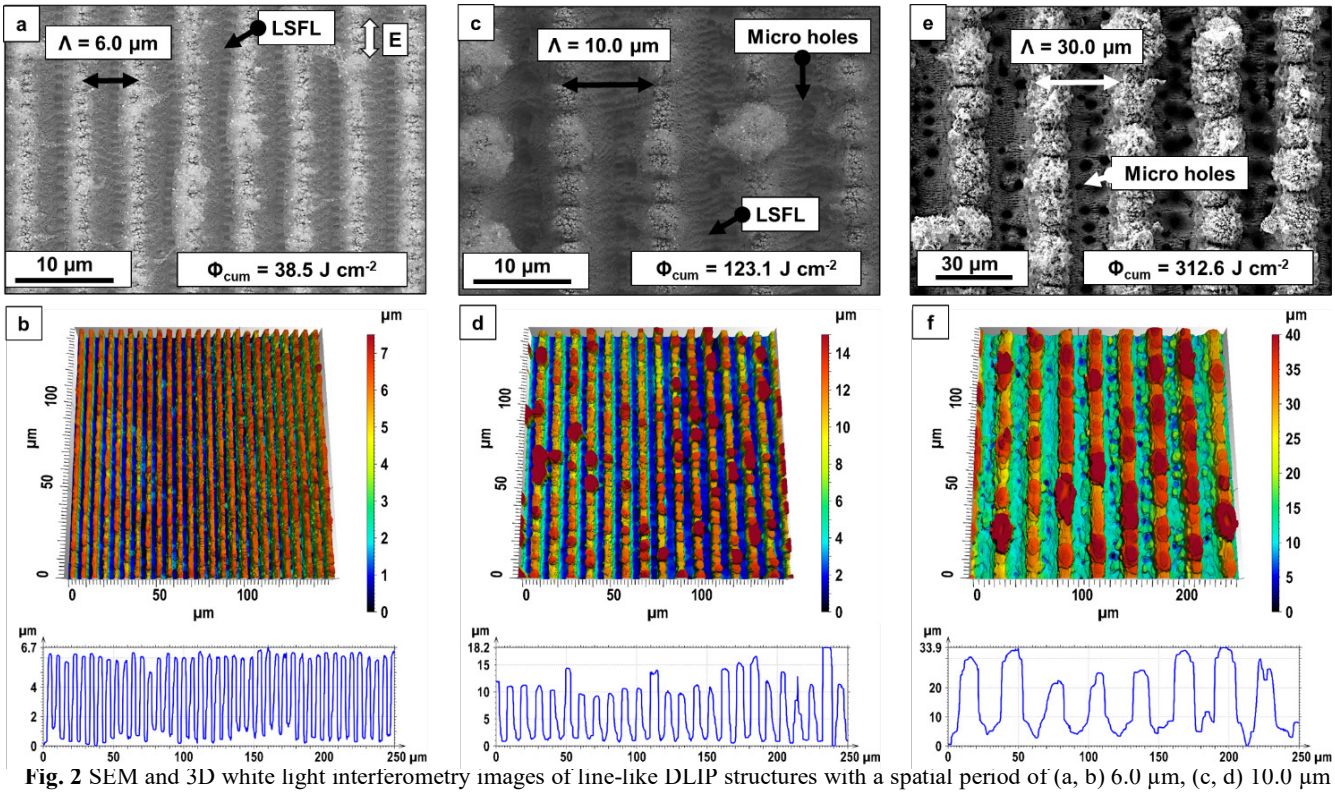

Fig. 2 SEM and 3D white light interferometry images of line-like DLIP structures with a spatial period of (a, b) 6.0 µm, (c, d) 10.0 µm and (e, f) 30.0 µm and AR = 1.0. Extracted profiles are shown below each sub-figure. The cumulated fluence (Φ_{cum}) is displayed in the corresponding labels above.

Table 1 Surface free energy (SFE) of used test liquids at 298 K.

Liquids	SFE [mN m^{-1}]	Polar γP [mN m^{-1}]	Dispersive γD [mN m^{-1}]
Di-water	72.8	51.0	21.8
Diiodomethane	50.8	0.0	50.8

3. Results and discussion

3.1 High aspect ratio DLIP structures

Periodic line- and cross-like structures with spatial periods (Λ) of 6.0, 10.0, 30.0 µm and aspect ratios (AR) of 0.3, 0.6, 1.0 were fabricated by DLIP. **Figure 2** displays exemplary SEM and white-light interferometry images of the fabricated DLIP line-like structures with an aspect ratio (AR) of 1.0. In **Figure 2a** well-defined parallel lines with a spatial period of 6.0 µm are observed. Superimposed on the DLIP pattern, sub-wavelength ripples, identified as Low Spatial Frequency LIPSS (LSFL), are clearly visible and oriented perpendicular to the laser polarization. The corresponding WLI image confirms a homogeneous surface modulation with peak-to-valley heights of approximately 6.1 ± 0.4 µm, indicating a regular and symmetric ablation profile.

In contrast, an increase in spatial period to 10.0 µm led to less regular line-like textures, with visible LSFL and emerging micro-holes at positions of maxima interference due to the higher cumulated fluence (**Figure 2c**). Moreover, in **Figure 2d** non-uniform material re-deposition is visible on the structure peaks of the DLIP pattern.

Figure 2e, displays line-like structures with a 30.0 µm period featuring a periodic array of laser-induced micro-holes inside the valleys of the DLIP pattern. Furthermore, significant material re-deposition becomes evident not only at the interference maxima positions but also at the minima.

The resulting prominent accumulation of re-deposited material and the appearance of the micro-hole sub-structure can be attributed to the higher cumulative fluence (312.6 J cm^{-2}) in comparison with the textures in **Figure 2a-d**.

Together, the SEM and WLI images demonstrate how increasing spatial period and fluence lead to more complex morphologies, evolving from smooth line-like patterns to hierarchical, porous surface textures.

The complete set of 3D WLI and SEM images for the produced line- and cross-like hierarchical DLIP structures can be found in **Appendix A, B, C, D**. Further details regarding the structure formation process can be found elsewhere [33].

3.2 Temporary evolution of static wetting properties

To determine the relation between the structure topography and the wetting behavior, static water contact angle (WCA) measurements have been carried out over 220 days.

Figure 3 shows the time-dependent development of the static water contact angle for all line- and cross-like DLIP treated samples with aspect ratios of 0.3, 0.6 and 1.0. The dashed line represented the WCA of the untreated reference with a mean value of 69.1° ± 4.3°.

Directly after laser structuring, the water droplets placed on the samples tended to wet the whole structured area, exhibiting either superhydrophilic (WCA < 10°) or hydrophilic behavior (10° < WCA < 90°). In particular, line-like textures showed a strong directional spreading of the liquid droplet along the grooves (**Appendix E**). The low initial WCA were

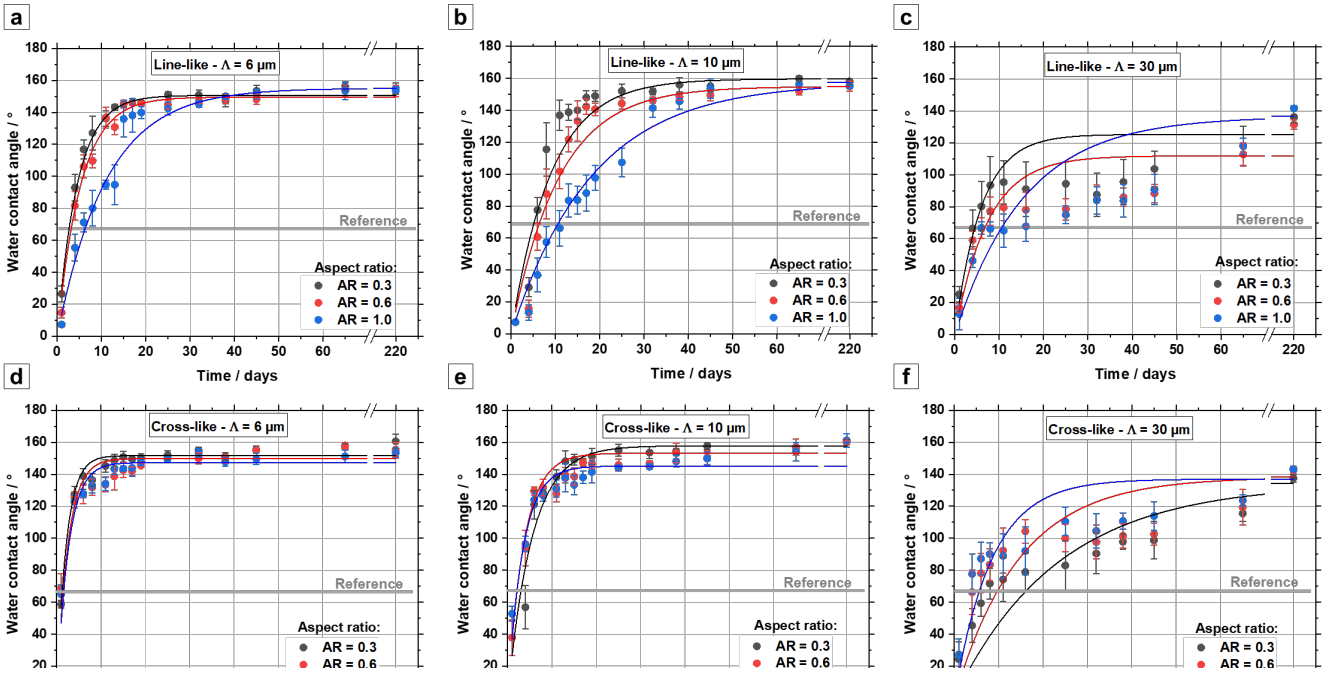

Fig. 3 Time-dependent development of the static water contact angle over a period 220 days for line- and cross-like DLIP structures with aspect ratio (AR) of 0.3, 0.6 and 1.0 and spatial periods (Λ) of (a, d) 6.0 µm, (b, e) 10.0 µm, (c, f) 30.0 µm.

attributed to the presence of an iron oxide layer, consisting of numerous active polar sites, which formed as a result of the laser-material interaction under ambient conditions [34].

Over time, the WCA increased for all samples, which is attributed to the dissociative adsorption of CO_2 from the ambient air. This process resulted in the formation of a non-polar carbon layer, which promoted hydrophobicity. Such effect has already been described by Kietzig et. al., who performed X-ray Photoelectron Spectroscopy (XPS) analysis revealing a continuous increase in carbon content over time [35]. As a consequence, the generated non-polar layer on the substrate surface reduces the wettability due to their low interaction with the polar forces and the limited amount of hydrogen bonds with the water molecules, thereby increasing the water contact angle [36].

The time-dependent change in surface chemistry combined with the generated microstructure provided surfaces with strong hydrophobic properties for all textures. Particularly, the samples textured with either cross-like or line-like structures with spatial periods of 6.0 or 10.0 µm showed a superhydrophobic characteristic in terms of WCA > 150°, regardless of the aspect ratio.

The observed hydrophobic behavior is assumed to be controlled by the wetting state defined by Cassie-Baxter theory [37], which states that air cushions separate the water droplet and the texture's valleys, while the liquid sits on the peaks of the DLIP pattern. For the spatial period (Λ) of 30.0 µm, the observed lower static water contact angle (130° < WCA < 150°) indicated that the water droplet was able to partially penetrate into the valleys of the DLIP features, thus increasing the wetted area and reducing the WCA.

Additionally, the measurements in **Figure 3** confirmed that the wetting state of cross-like and line-like patterns with spatial periods of 6.0 and 10.0 µm are stable, at least until day 220 from fabrication, once they reach the steady state, i.e., typically between 20 and 45 days after fabrication. For the samples with a spatial period of 30.0 µm the corresponding WCA exhibited a steady increase to values between 120° and 140° over 220 days.

The evolution of the WCA could be approximated with the exponential saturation equation proposed by Kietzig (Equation 3) [36]

$$\theta = \theta_{max} \cdot \left(1 - e^{\frac{-t}{\lambda_{WCA}}}\right), \quad (3)$$

where θ_{max} is the maximum contact angle after 220 days and λ_{WCA} represents a time constant, which refers to the time until 63.2% of the maximum contact angle value is reached. By fitting the experimental data with Equation 3 (lines in **Figure 3**), the regression coefficient λ_{WCA} could be calculated and it is summarized in **Table 2** for all manufactured textures.

As observed in **Table 2**, the regression coefficient (λ_{WCA}) tends to increase with AR for all line-like structures. This observation can be attributed to the differences in cumulated laser fluences (Φ_{cum}) applied during the laser processing. Structures with smaller aspect ratios were fabricated using lower cumulated laser fluences and exhibited a more rapid increase in WCA (characterized by a smaller time constant, λ_{WCA}) compared to those with higher aspect ratios, which were produced using higher cumulated fluences. Regardless of the applied spatial period, processing with low cumulated fluences resulted in a reduced level of oxidation on the steel substrate. Consequently, the number of active polar sites was

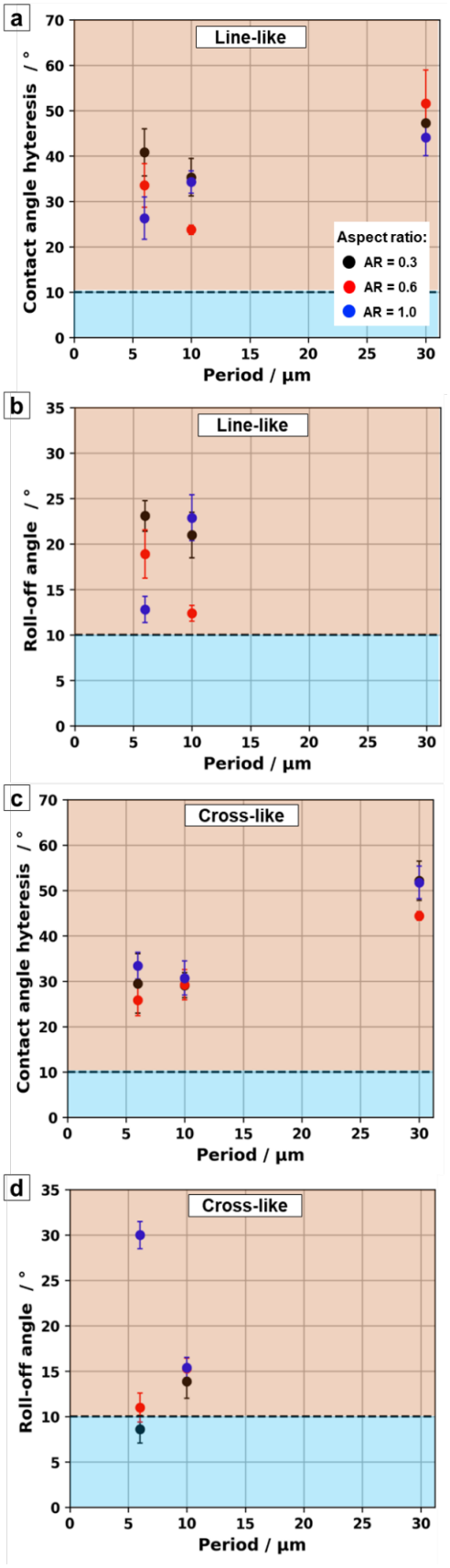

Fig. 4 (a, c) Contact angle hysteresis (CAH) and (b, d) roll-off angles ($\theta_{Roll\text{-}off}$) 220 days after the laser treatment for the line- and cross-like DLIP structures as a function of spatial period (Λ) and aspect ratio (AR).

lower for these structures, compared to those with high aspect ratios, favoring the transition to the hydrophobic state over time. On the contrary, there is no clear correlation between the time constant λ_{WCA} and AR over the three studied spatial periods (**Table 2**). In case of the samples with spatial period of 6.0 and 10.0 µm, the cross-like patterns showed practically constant regression coefficients. However, for the spatial period of 30.0 µm the regression coefficient became smaller with increasing AR. A more detailed surface chemical analysis is still needed to shed light into this unexpected behavior, which will be conducted in a future study.

Table 2 Time dependent regression coefficient λ_{WCA} for line- and cross-like DLIP structures with spatial periods (Λ) of 6.0, 10.0, 30.0 µm and different aspect ratios (AR).

Period Λ [µm]	Aspect ratio AR	λ_{WCA} (Line-like) [days]	λ_{WCA} (Cross-like) [days]
6.0	0.3	4.5	2.1
	0.6	5.2	2.4
	1.0	11.1	2.6
10.0	0.3	9.1	5.4
	0.6	10.8	3.6
	1.0	18.4	3.4
30.0	0.3	5.9	23.3
	0.6	7.4	14.6
	1.0	15.7	8.3

3.3 Dynamic wettability analysis

To further assess the wetting properties, the static contact angle hysteresis (CAH) and the roll-off angle ($\theta_{Roll\text{-}off}$) were measured on the DLIP-treated samples 220 days after laser texturing. For obtaining the CAH, regular sessile drops deposited on the texture's surfaces were imaged by the contact angle measurement device, while the droplets were enlarged and reduced to obtain the advancing (θ_{Adv}) and receding (θ_{Rec}) contact angles (listed in **Appendix F**). The hysteresis values as well as the roll-off angles after 220 days are summarized in **Figure 4** for all samples.

There is an agreed consensus in the scientific community that a surface is considered superhydrophobic when the WCA is larger than 150°, combined with CAH smaller than 10° and a roll-off angle ($\theta_{Roll\text{-}off}$) below 10° [38]. For this purpose, the individual diagrams in **Figure 4** were divided into the areas corresponding to hydrophobic (light orange) and superhydrophobic (light blue) wetting state. Considering the hysteresis values in **Figure 4a, c** it became noticeable that none of the laser-textured surfaces were able to transition into the superhydrophobic regime.

According to Bhushan and Nosonovsky, a relatively high hysteresis paired with high static water contact angles observed in hierarchical structures suggested a complex wetting state, where individual micro- and nanoscale features are either fully or partially wetted. The size and distribution of these micro- and nanostructures significantly influences the ability of the interface to pin the contact line of a water droplet [39]. Consequently, it is here hypothesized that varying the spatial period (Λ) and texture type resulted in different wetting states.

For instance, in the case of line- and cross-like structures with a spatial period of Λ = 30.0 µm, the contact angle hysteresis (CAH) was approximately 60% higher than on the surfaces with the other periods. This observation suggests a rose petal effect [40], in which the microstructure beneath the droplet is fully wetted, while the nanostructures are only partially wetted, irrespective of the aspect ratio. As a result, the DLIP grooves contributed to high droplet adhesion, preventing the droplet from rolling off the surface, whereas the nanoscale structures induced high static water contact angles.

As shown in **Figures 4b** and **4d**, droplets deposited on all samples with periods of 6.0 and 10.0 µm have rolled off the surface at the measured $\theta_{Roll\text{-}off}$. Specifically, the roll-off angles for both line-like and cross-like DLIP textures ranged between 12°–23° and 8°–30°, respectively. A correlation between CAH and roll-off angle was evident, as patterns with the smallest CAH also allowed droplets to roll off at the lowest tilting angles. This behavior suggests that the liquid does not infiltrate significantly the structure valleys, forming air pockets that reduce contact area and droplet adhesion. The reason for this might be the increased surface area combined with a lower density of support points for the droplet to rest upon. This confirms a Cassie-Baxter wetting state for both line- and cross-like textures. Interestingly, cross-like structures with Λ = 6.0 µm and AR = 0.3 had the lowest roll-off angle of 8.4°, which can be further utilized for self-cleaning applications [41].

3.4 Surface free energy analysis

Additionally, the surface free energy (SFE) was measured for the laser-structured surfaces. For this purpose, the OWRK method was applied to determine the SFE based on static contact angle measurements of deionized water and diiodomethane droplets deposited on the surfaces, allowing the calculation of the polar (γP) and dispersive (γD) components. These contact angles were recorded 220 days after the laser structuring experiments.

Figure 5 displays on the left axis the obtained dispersive (γD) and polar (γP) components, and total surface free energy (SFE), and on the right axis the average contact angles for each test liquid as a function of spatial period and the aspect ratio. The SFE of the reference steel surface (46.4 ± 0.3 mN m^{-1}) aligned closely with values reported in the literature, confirming the consistency of these measurements [42].

Compared to the reference, a general increase in the surface free energy can be observed in all samples as a result of the DLIP treatment. The values of the surface energy vary between 60 and 70 mN m^{-1}, for all samples with a spatial period of 6.0 and 10.0 µm.

For the DLIP-treated samples, it should be noted that the dispersive component constitutes the main part of the surface tension and is primarily responsible for the increase in SFE. This promotes the tendency of non-polar liquids to wet and spread extensively on the surfaces of the patterned samples. The high wettability by diiodomethane and the resulting low contact angles can be attributed to prevailing intermolecular interactions, which are influenced by the presence of oxides on the treated surfaces, leading to the formation of chemical species with dispersive character within the surface boundary layer [43].

A different behavior is observed for the polar component of the free surface energy. The results shown in **Figure 5** indicate a reduction in the polar contribution compared to the

untreated reference, which is interpreted as a direct consequence of the accumulation of non-polar compounds after laser processing. As a result, polar interactions contribute only minimally to the surface tension, resulting in poor wettability and high contact angles for polar liquids such as water.

As shown in **Figure 5**, structures with spatial periods of 6.0 and 10.0 µm exhibited larger polar components than the samples with $\Lambda = 30.0$ µm, despite having significantly higher water contact angles. It needs to be taken into account that the surface patterns with $\Lambda = 6.0$ µm and $\Lambda = 10.0$ µm exhibit a Cassie–Baxter wetting behavior, where the water droplet partially rests on air pockets trapped between structural peaks. However, this condition does not necessarily imply that the surfaces with smaller spatial periods are less polar. In fact, due to the smaller spatial periods, these surfaces have a higher density of structural peaks, which could locally expose more polar functional groups (e.g., hydroxyl groups). As a result, even though the droplet interacts with less of the actual solid surface (due to air entrapment), the surface still presents a higher degree of chemical polarity, which is reflected in the larger polar component of the surface free energy. Kuznetsov et al. noted in this context that polar interactions are not only defined by strong bonds between molecules (e.g., hydrogen, covalent, and dipole bonds) but are also influenced by the prevailing size and distribution of roughness features on the surface [44].

The strong contrast between the low polar and high non-polar components of the SFE observed on all structured samples can further enable new applications. Namely, in addition to the observed water-repellency, the high dispersive component might attract oils. Such opposite behavior can be exploited for surfaces that can separate water from oil [45]. Additional experiments should be performed on the DLIP-treated surfaces to confirm this hypothesis.

4. Conclusion

The application of picosecond DLIP has been successfully demonstrated for the fabrication of high aspect ratio line- and cross-like microstructures on stainless steel (SS1.4301) using an innovative optical head based on two-beam interference optics.

The wettability of line- and cross-like DLIP surfaces with AR values of 0.3, 0.6, and 1.0 was characterized over a period of 220 days, revealing a transition from initial hydrophilic states to strongly hydrophobic states depending on the spatial period. Specifically, surfaces with $\Lambda = 30.0$ µm became hydrophobic with WCA < 150°, while those with $\Lambda = 6.0$ and 10.0 µm transitioned to a superhydrophobic regime in terms of static WCA. Moreover, laser-structured surfaces exhibited different contact angle hysteresis (CAH) and roll-off behavior. Structures with largest spatial period $\Lambda = 30.0$ µm demonstrated a rose petal effect, where the microstructure caused strong adhesion of the water droplet to the surface. In turn, a reduction in spatial period to $\Lambda = 6.0$ and 10.0 µm reduced the wettability and adhesion of water droplets to the surface allowing the droplets to roll-off the surface at tilting angles between 8 and 30° indicating a Cassie-Baxter wetting regime. In general, it was observed that the main texture parameter controlling the long-term wetting state is the DLIP period, whereas the aspect ratio or texture type did not affect consistently the wetting characteristics.

The results obtained in this study can be further exploited for many technically relevant applications such as surfaces with self-cleaning, oil/water separation, anti-icing, or anti-corrosion functionalities.

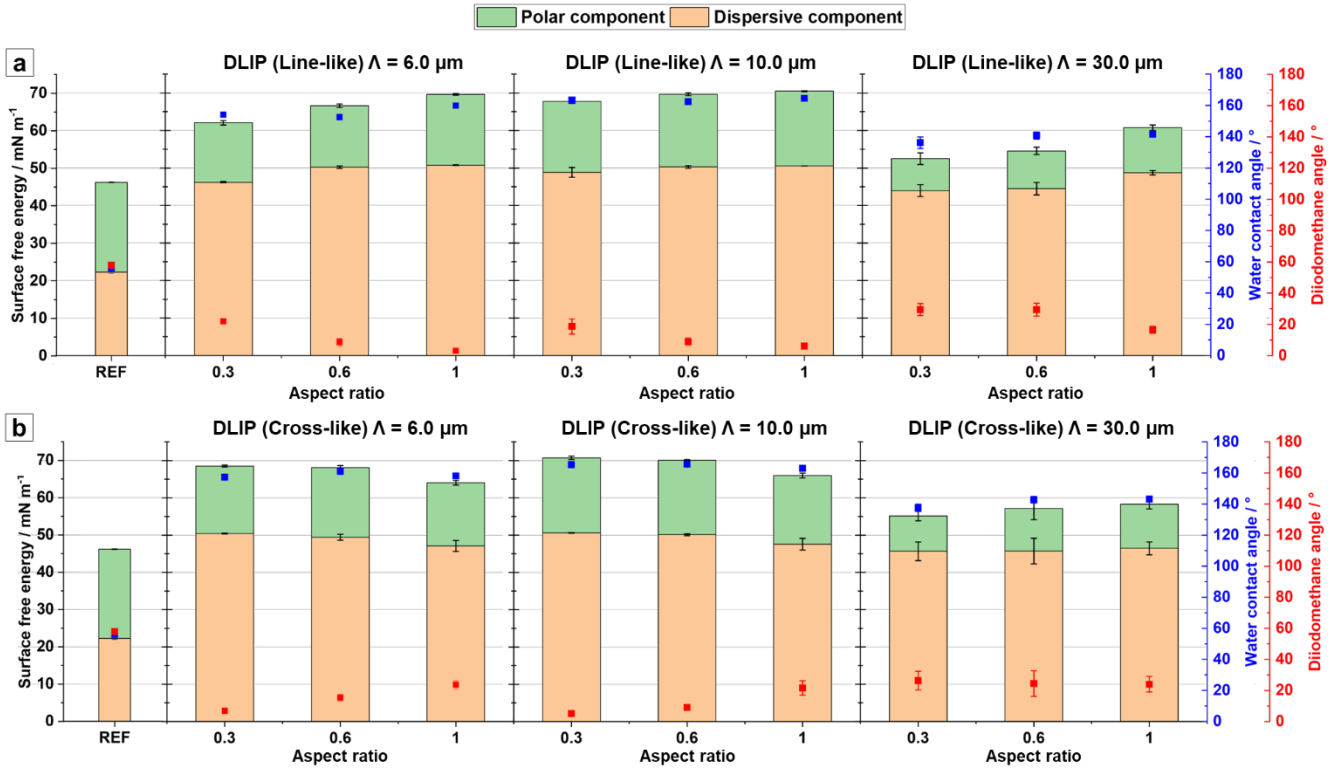

Fig. 5 Surface free energy (SFE) and corresponding dispersive (γD) and polar (γP) components and corresponding water- and diiodomethane contact angles after 220 days for (a) line- and (b) cross-like DLIP structures with aspect ratio (AR) of 0.3, 0.6 and 1.0 and spatial periods (Λ) of 6.0 µm, 10.0 µm, 30.0 µm.

Acknowledgments and Appendixes

This project was funded by the European Regional Development Fund (ERDF) and co-financed under taxation on the basis of the budget adopted by the members of the Saxon State Parliament. This publication is part of the M-ERA.Net project M-LUGE and is co-financed with tax funds on the basis of the budget passed by the Saxon State Parliament.

Appendix A

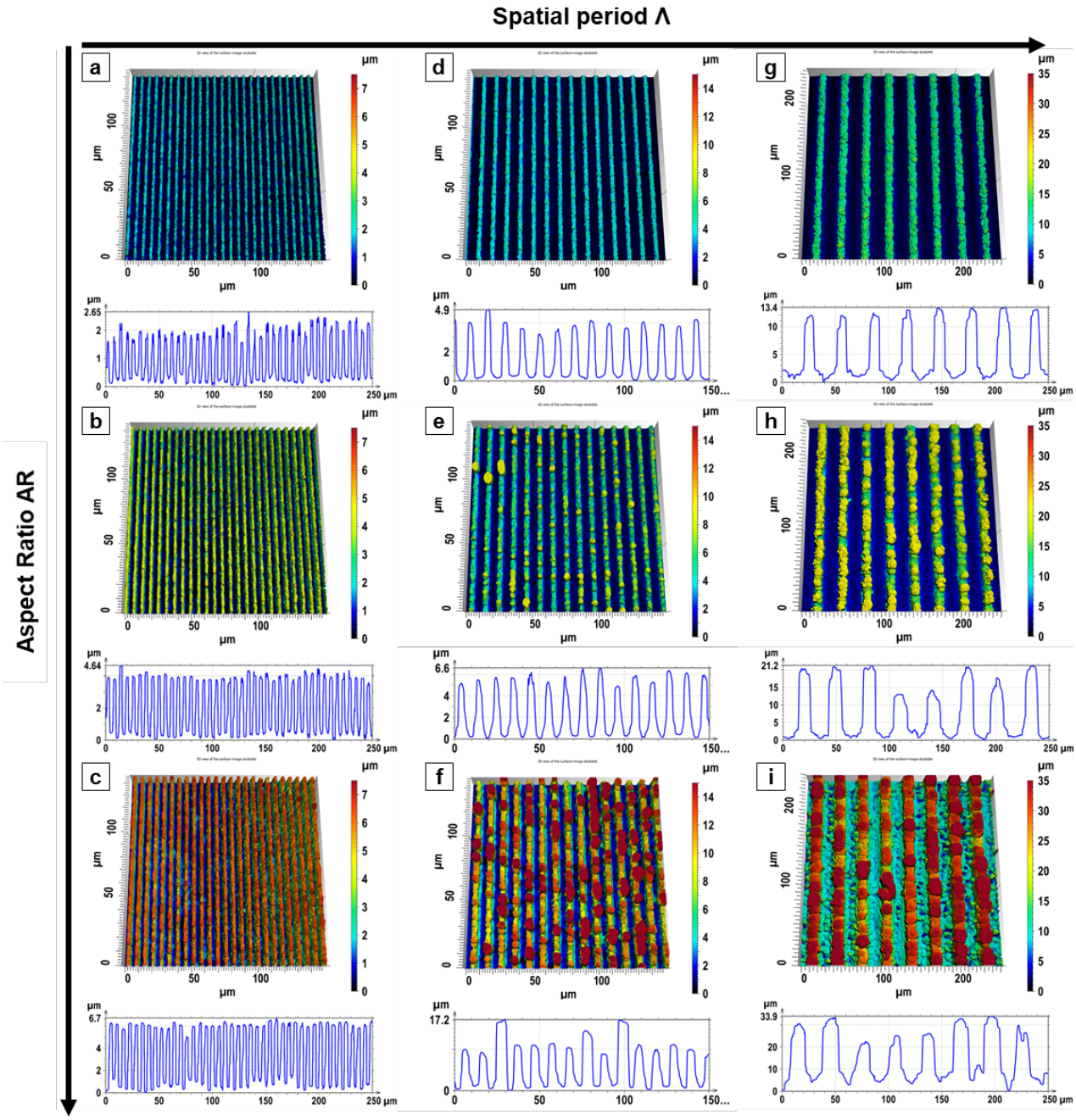

Appendix A 3D topography images taken by WLI of line-like DLIP structures with a spatial period of (a-c) 6.0 µm, (d-f) 10.0 µm and (g-i) 30.0 µm with AR = 0.3, 0.6, 1.0. Also, extracted profiles are shown below each figure.

Appendix B

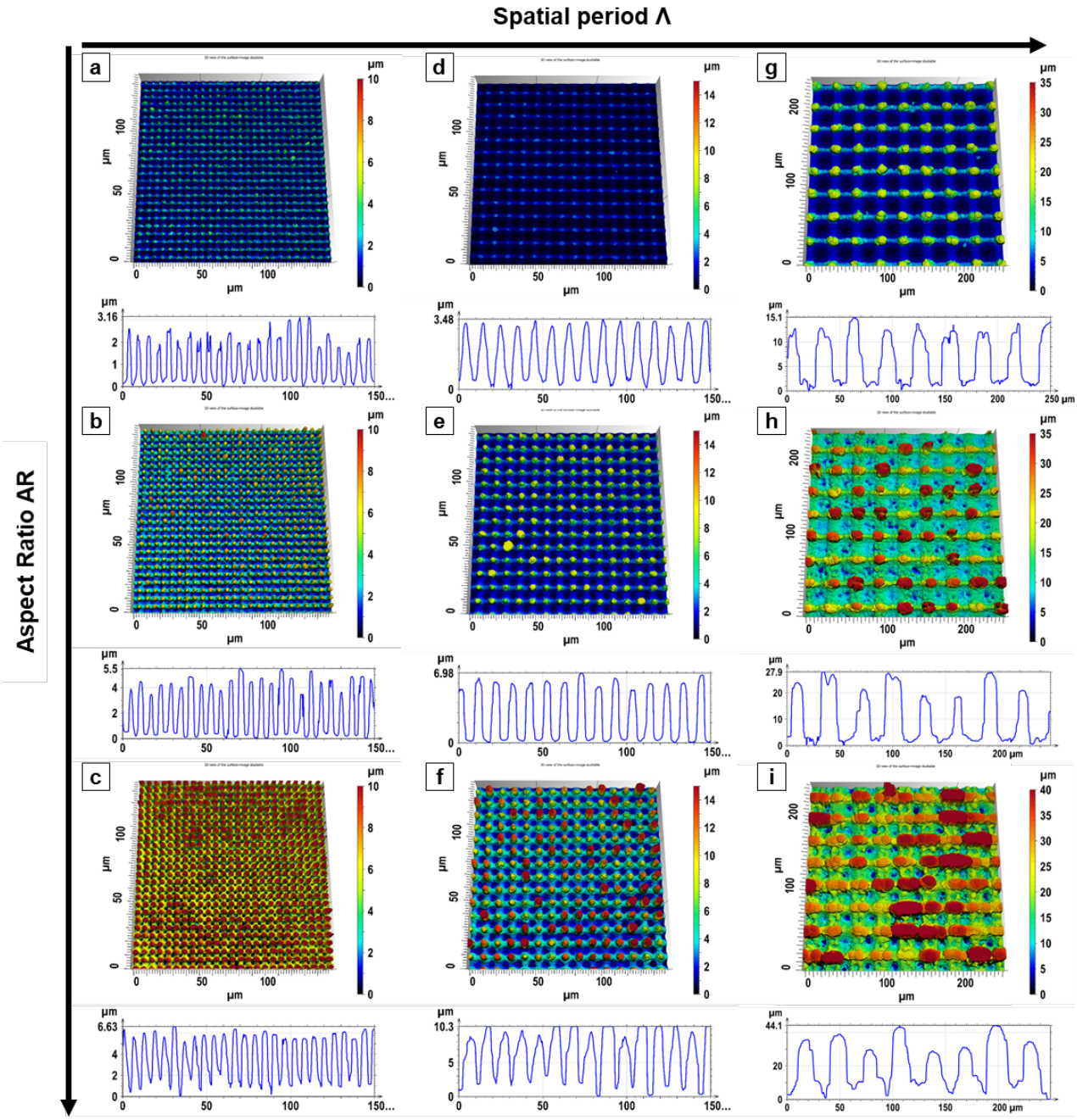

Appendix B 3D topography images taken by WLI of cross-like DLIP structures with a spatial period of (a-c) 6.0 µm, (d-f) 10.0 µm and (g-i) 30.0 µm with AR = 0.3, 0.6, 1.0. Also, extracted profiles are shown below each figure.

Appendix C

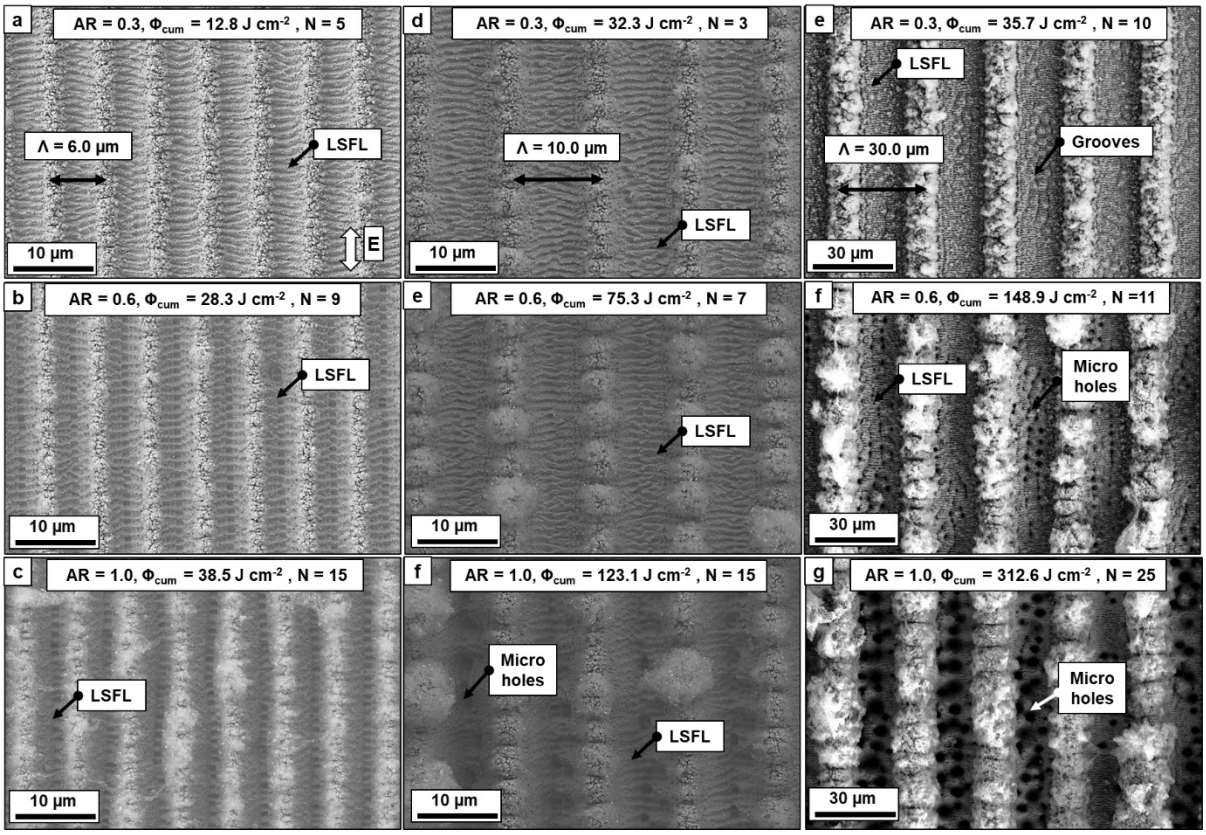

Appendix C SEM images of line-like DLIP structures with a spatial period of (a-c) 6.0 µm, (d-f) 10.0 µm and (g-i) 30.0 µm with AR = 0.3, 0.6, 1.0. The aspect ratio (AR) cumulated laser fluence (Φ_{cum}) and the total number of applied passes (N) are displayed in the corresponding labels.

Appendix D

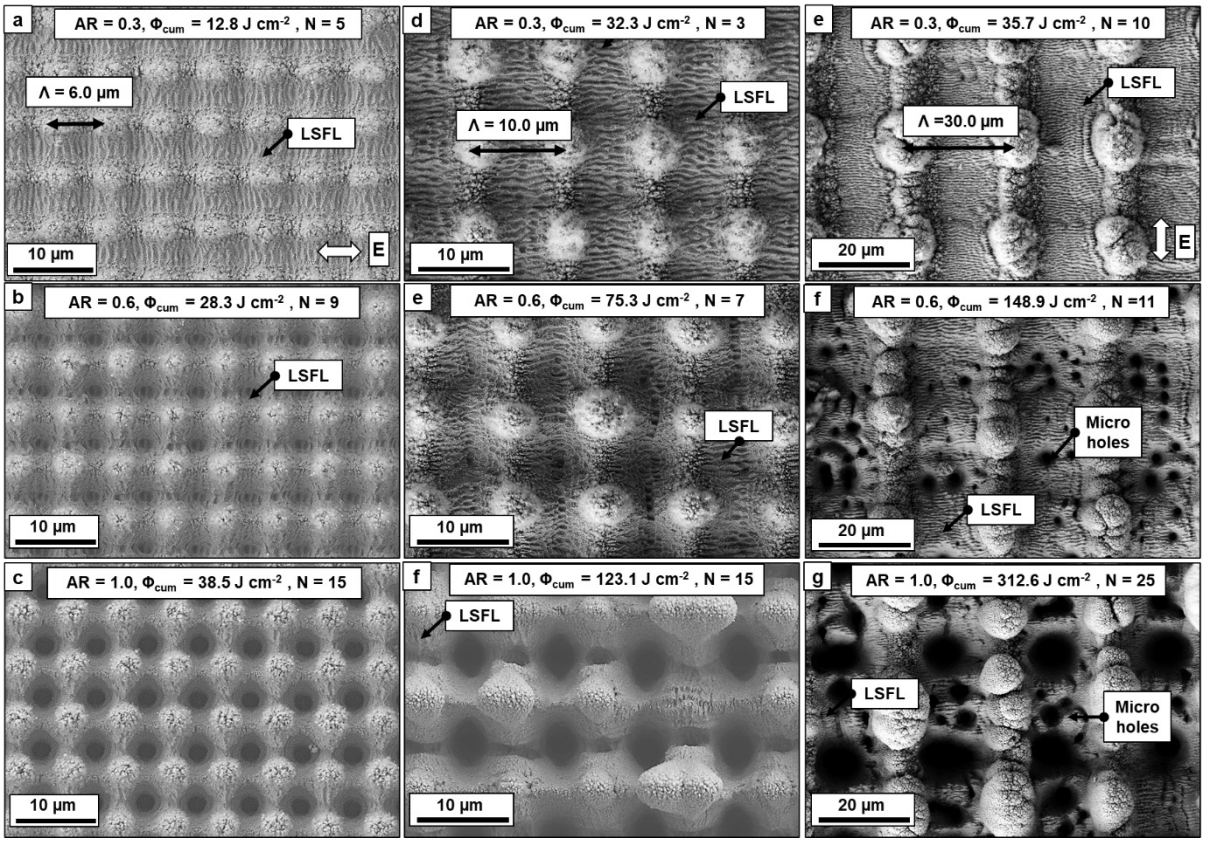

Appendix D SEM images of cross-like DLIP structures with a spatial period of (a-c) 6.0 µm, (d-f) 10.0 µm and (g-i) 30.0 µm with AR = 0.3, 0.6, 1.0. The aspect ratio (AR) cumulated laser fluence (Φ_{cum}) and the total number of applied passes (N) are displayed in the corresponding labels.

Appendix E

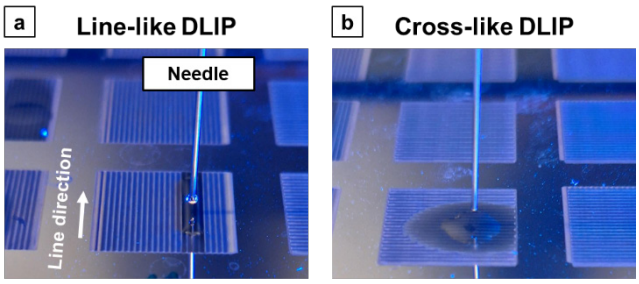

Appendix E Exemplary optical images of spreading behavior for (a) line- and (b) cross-like DLIP patterns directly after laser texturing.

Appendix F

Table 3 Resulting advancing (θ_{Adv}) and receding (θ_{Rec}) water contact angles for the line- and cross-like DLIP structures with Λ = 6.0, 10.0, 30.0 µm and different aspect ratios (AR) 220 days after laser texturing.

Period Λ [µm]	Aspect ratio AR	θ_{Adv} (Line-like) [°]	θ_{Rec} (Line-like) [°]	θ_{Adv} (Cross-like) [°]	θ_{Rec} (Cross-like) [°]
6.0	0.3	169.4 ± 2.0	128.6 ± 6.2	174.2 ± 1.2	144.7 ± 6.3
	0.6	171.2 ± 1.3	137.6 ± 5.0	172.7 ± 3.0	146.8 ± 6.4
	1.0	171.6 ± 2.1	145.3 ± 3.4	171.6 ± 3.2	138.1 ± 2.4
10.0	0.3	171.2 ± 5.3	135.8 ± 4.8	168.8 ± 3.5	139.6 ± 3.6
	0.6	170.4 ± 3.0	146.6 ± 3.1	167.0 ± 2.5	137.8 ± 4.2
	1.0	170.7 ± 1.8	136.4 ± 3.8	169.8 ± 2.7	139.1 ± 2.7
30.0	0.3	160.6 ± 9.7	111.1 ± 4.4	167.2 ± 1.9	115.0 ± 5.4
	0.6	160.3 ± 7.4	109.6 ± 6.4	162.2 ± 0.8	117.8 ± 1.6
	1.0	154.7 ± 6.7	110.6 ± 6.4	168.2 ± 1.8	116.4 ± 2.8

References

[1] P. Boillot and J. Peultier: Procedia Eng., 84, (2021) 309.
[2] S. K. Sethi and G. Manik: Polym.-Plast. Technol. Eng., 57, (2018) 1932.
[3] G. Liu, T. Zhao, H. Fei, F. Li, W. Guo, Z. Yao, and Z. Feng: Constr. Build. Mater., 409, (2023) 134084.
[4] Q. Xu, W. Zhang, C. Dong, T. S. Sreeprasad, and Z. Xia: J. R. Soc. Interface, 13, (2016) 20160300.
[5] P. Chevallier, S. Turgeon, C. Sarra-Bournet, R. Turcotte, and G. Laroch: ACS Appl. Mater. Interfaces, 3, (2011) 750.
[6] J. Zhao, L. Ma, W. Millians, T. Wu, and W. Ming: ACS Appl. Mater. Interfaces, 8, (2016) 8737.
[7] I. R. Durán and G. Laroche: Prog. Mater. Sci., 99, (2019) 106.
[8] A. Thakur, A. Kumar, S. Kaya, R. Marzouki, F. Zhang, and L. Guo: Coat., 12, (2022) 1459.
[9] S. M. Matar, A. Yousef, A. M. Bastaweesy, I. Y. Quedsieh, and I. M. Maafa: Coat., 14, (2024) 1518.
[10] M. Zhang, S. Feng, L. Wang and Y. Zheng: Biotribology, 5, (2016) 31.
[11] C. Florian, S. V. Kirner, J. Krüger, and J. Bonse: J. Laser Appl., 32, (2020) 022063.
[12] Z. Chen, J. Yang, H. Liu, Y. Zhao, and R. Pan: Int. J. Adv. Manuf. Technol., 119, (2022) 6919.
[13] K. Yu, H. Shi, P. Zhang, Z. Yu, H. Yan, and Q. Lu: J. Mater. Sci., 59, (2024) 1819.
[14] A. F. Lasagni: Adv. Opt. Technol. 2017, *6*, 265.
[15] F. Ränke, R. Baumann, B. Voisiat, and A. F. Lasagni: Mater. Lett. X, 14, (2022) 100144.
[16] V. Lang, B. Voisiat, T. Kunze, and A. F. Lasagni: Adv. Eng. Mater., 21, (2019) 1900151.
[17] A. F. Lasagni, T. Roch, J. Berger, T. Kunze, V. Lang, and E. Beyer: Proc. SPIE, Vol. 9351, (2015) 248.
[18] S. Indrišiūnas, B. Voisiat, M. Gedvilas, and G. Račiukaitis: J. Laser Appl., 29 (2017) 011501.
[19] M. Bieda, M. Siebold, and A. F. Lasagni: Appl. Surf. Sci., 387, (2016) 175.
[20] M. Bieda, E. Beyer, and A. F. Lasagni: J. Eng. Mater. Technol., 132, (2010) 3.
[21] V. Vercillo, S. Tonnicchia, J.-M. Romano, A. García-Girón, A. I. Aguilar-Morales, S. Alamri, S. S. Dimov, T. Kunze, A. F. Lasagni, and E. Bonaccurso: Adv. Funct. Mater., 30, (2020) 1910268.
[22] F. Schell, S. Alamri, A. Hariharan, A. Gebert, A. F. Lasagni, and T. Kunze: Mater. Lett., 306, (2022) 130920.
[23] R. Han, Y. Zhang, Q. Jiang, L. Chen, K. Cao, S. Zhang, D. Feng, Z. Sun, and T. Jia: OES., 3, (2024) 230013.
[24] Z. Lin, L. Ji, B. Zhou, W. Sun, D. Yang, F. Yang, and T.Yao: Mater. Today Phys., 51, (2025) 101636.
[25] A. I. Aguilar-Morales, S. Alamri, B. Voisiat, T. Kunze, and A. F. Lasagni: Materials, 12, (2019) 2737.
[26] B. Raillard, J. Rémond, E. Ramos-Moore, N. Souza, C. Gachot, and F. Mücklich: Adv. Eng. Mater., 15, (2013) 341.
[27] A. Peter, A. H. A. Lutey, S. Faas, L. Romoli V. Onuseit, and T. Graf: Opt. Laser Technol., 123, (2020) 105954.
[28] A. I. Aguilar-Morales, S. Alamri, and A. F. Lasagni: J. Mater. Process. Technol., 252, (2018) 313.
[29] F. Schell, S. Alamri, T. Steege, C. Zwahr, T. Kunze, and A. F. Lasagni: Surf. Coat. Technol., 447, (2022) 128869.
[30] H. Shimada, K. Watanabe, and M. Yamaguchi, J. Laser Micro Nanoeng., 16, (2021) 94.
[31] F. M. Fowkes: Ind. Eng. Chem., 56, (1964) 40.
[32] S. Razi, K. Madanipour, and M. Mollabashi: J. Laser Appl., 27, (2015) 042006.
[33] F. Ränke, M. Sallese, M. Soldera, I. Tabares, F. Soldera, and A. F. Lasagni: Adv. Eng. Mater., (2025) 22500570.
[34] A.-M. Kietzig, M. Negar Mirvakili, S. Kamal, P. Englezos, and S. G. Hatzikiriakos: J. Adhes. Sci. Technol., 25, (2011) 2789.
[35] A.-M. Kietzig, S. G. Hatzikiriakos, and P. Englezos: Langmuir, 25, (2009) 4821.
[36] M. M. Gentleman and J. A. Ruud: Langmuir, 26 (2010), 1408.
[37] H. Yildirim Erbil and C. Elif Cansoy: Langmuir, 24, (2009) 24.
[38] A. Marmur, C. Della Volpe, S. Siboni, A. Amirfazli, and J. W. Drelich: Surf. Innov., 5, (2017) 3.
[39] B. Bhushan and M. Nosonovsky: Philos. Trans. R. Soc. Math. Phys. Eng. Sci., 368, (2010) 1929.
[40] H. Lin and L. Chen: J. Colloid Interface Sci., 603, (2021) 539.
[41] Z. Chang and Y. Lu, J. Dispers: Sci. Technol., 43, (2022) 1099.
[42] C. I. Pereni, Q. Zhao, Y. Liu, and E. Abel: Colloids Surf. B Biointerfaces, 48, (2006) 143.
[43] D. H. Kaelble: J. Adhes., 2, (1970) 66.
[44] G. V. Kuznetsov, A. G. Islamova, E. G. Orlova, A. S. Ivashutenko, I. I. Shanenkov, I. Y. Zykov, and D. V. Feoktistov: Surf. Coat. Technol., 422, (2021) 127518.
[45] C. Chen, D. Wenig, A. Mahmood, S. Chen, and J. Wang: ACS Appl. Mater. Interfaces., 11, (2019) 11.

(Received: June 4, 2025, Accepted: July 24, 2025)